such a double-gyroid phase from the rigid and symmetric giant tetrahedron **3a** reflects the ubiquity of the gyroid structure, implying the subtle influence of the slightly different volume fractions and interactions on the selective assembly of these giant tetrahedra (Fig. 4G).

Giant tetrahedra **4a** to **4c** failed to crystallize in similar solvent evaporation processes because of the low volume fraction of BPOSS cages that does not favor the formation of continuous 2D flat crystals (fig. S8). At such a volume fraction, an inverse spherical phase such as bcc or A15 was expected. However, after thermal annealing at 130°C, only ordered hexagonal cylinder phases were observed in **4a** to **4c**, as revealed by the q value ratio of $1:\sqrt{3}:\sqrt{4}$ in their SAXS patterns (fig. S8B, Fig. 4C, and fig. S8C for **4a**, **4b**, and **4c**, respectively) and the honeycomb-like hexagonal structure observed in BF TEM images (Fig. 4F). In the proposed schematic packing model of **4a** to **4c** (Fig. 4H), BPOSS cages are wrapped into centers of the columns while hydrophilic POSS cages with strong collective hydrogen bonding form the continuous matrix. In sharp contrast to the packing of **2a** to **2c** at higher temperatures, **4a** to **4c** tend to maximize the contacts of hydrophilic POSS cages (and thus the extent of collective hydrogen-bonding formation), which substantially minimizes the overall free energy of the system.

Symmetry breaking on accurately controlled positional interactions of nanosized giant tetrahedra has been used to construct the Frank-Kasper A15 phase and other ordered supramolecular lattices. The diverse self-assembly behaviors of these giant tetrahedra reveal that rigid, single-component soft-matter systems offer potential for building supramolecular "metal alloy analogs." The subtle competition between the persistent molecular geometry and the deformability driven by interaction terms dictates the selective assembly of the giant tetrahedra. Because of the "click" synthesis, this system is highly tunable in terms of core structure, nanoparticle functionality, and feature size. The concepts and formation mechanisms of these supramolecular structures could be extended to other giant-polyhedra molecules with different topologies and chemical compositions.

REFERENCES AND NOTES

1. M. D. Graef, M. E. Mchenry, *Structure of Materials: An Introduction to Crystallography, Diffraction and Symmetry* (Cambridge Univ. Press, Cambridge, ed. 2, 2012).
2. F. C. Frank, J. S. Kasper, *Acta Crystallogr.* **11**, 184–190 (1958).
3. F. C. Frank, J. S. Kasper, *Acta Crystallogr.* **12**, 483–499 (1959).
4. G. Ungar, X. Zeng, *Soft Matter* **1**, 95–106 (2005).
5. V. S. K. Balagurusamy, G. Ungar, V. Percec, G. Johansson, *J. Am. Chem. Soc.* **119**, 1539–1555 (1997).
6. X. Zeng *et al.*, *Nature* **428**, 157–160 (2004).
7. S. D. Hudson *et al.*, *Science* **278**, 449–452 (1997).
8. G. Ungar, Y. Liu, X. Zeng, V. Percec, W. D. Cho, *Science* **299**, 1208–1211 (2003).
9. K. Hayashida, T. Dotera, A. Takano, Y. Matsushita, *Phys. Rev. Lett.* **98**, 195502 (2007).
10. J. Zhang, F. S. Bates, *J. Am. Chem. Soc.* **134**, 7636–7639 (2012).
11. S. Lee, M. J. Bluemle, F. S. Bates, *Science* **330**, 349–353 (2010).
12. S. Lee, C. Leighton, F. S. Bates, *Proc. Natl. Acad. Sci. U.S.A.* **111**, 17723–17731 (2014).
13. S. Fischer *et al.*, *Proc. Natl. Acad. Sci. U.S.A.* **108**, 1810–1814 (2011).
14. D. V. Talapin *et al.*, *Nature* **461**, 964–967 (2009).
15. C. Xiao, N. Fujita, K. Miyasaka, Y. Sakamoto, O. Terasaki, *Nature* **487**, 349–353 (2012).
16. C. R. Iacovella, A. S. Keys, S. C. Glotzer, *Proc. Natl. Acad. Sci. U.S.A.* **108**, 20935–20940 (2011).
17. P. Ziherl, R. D. Kamien, *J. Phys. Chem. B* **105**, 10147–10158 (2001).
18. G. M. Grason, B. A. DiDonna, R. D. Kamien, *Phys. Rev. Lett.* **91**, 058304 (2003).
19. P. F. Damasceno, M. Engel, S. C. Glotzer, *Science* **337**, 453–457 (2012).
20. A. Haji-Akbari *et al.*, *Nature* **462**, 773–777 (2009).
21. D. B. Cordes, P. D. Lickiss, F. Rataboul, *Chem. Rev.* **110**, 2081–2173 (2010).
22. X. Yu *et al.*, *J. Am. Chem. Soc.* **134**, 7780–7787 (2012).
23. A. Dolbecq, E. Dumas, C. R. Mayer, P. Mialane, *Chem. Rev.* **110**, 6009–6048 (2010).
24. Y.-T. Lai, D. Cascio, T. O. Yeates, *Science* **336**, 1129 (2012).
25. W.-B. Zhang *et al.*, *Macromolecules* **47**, 1221–1239 (2014).
26. X. Yu *et al.*, *Proc. Natl. Acad. Sci. U.S.A.* **110**, 10078–10083 (2013).
27. K. Yue *et al.*, *Macromolecules* **45**, 8126–8134 (2012).
28. See supplementary materials on *Science* Online.
29. A. R. Bassindale *et al.*, *Dalton Trans.* **2003**, 2945–2949 (2003).
30. H. Liu *et al.*, *J. Am. Chem. Soc.* **136**, 10691–10699 (2014).
31. P. Ziherl, R. D. Kamien, *Phys. Rev. Lett.* **85**, 3528–3531 (2000).
32. D. Weaire, R. Phelan, *Philos. Mag. Lett.* **69**, 107–110 (1994).
33. V. Percec *et al.*, *J. Am. Chem. Soc.* **130**, 13079–13094 (2008).
34. Y. Li *et al.*, *J. Am. Chem. Soc.* **133**, 10712–10715 (2011).

ACKNOWLEDGMENTS

Supported by NSF grant DMR-1408872. We thank B. Lotz for helpful discussion. The MALDI-TOF MS analysis was assisted by K. Guo, C. Shi, and C. Wesdemiotis. Use of the Advanced Photon Source at Argonne National Laboratory was supported by the U.S. Department of Energy, Office of Science, Office of Basic Energy Sciences, under contract DE-AC02-06CH11357.

SUPPLEMENTARY MATERIALS

www.sciencemag.org/content/348/6233/424/suppl/DC1
Materials and Methods
Supplementary Text
Figs. S1 to S8
Table S1
References (*35*–*38*)

5 November 2014; accepted 2 March 2015
10.1126/science.aaa2421

METHANE CYCLING

Nonequilibrium clumped isotope signals in microbial methane

David T. Wang,[1,2] Danielle S. Gruen,[1,2] Barbara Sherwood Lollar,[3] Kai-Uwe Hinrichs,[4] Lucy C. Stewart,[5] James F. Holden,[5] Alexander N. Hristov,[6] John W. Pohlman,[7] Penny L. Morrill,[8] Martin Könneke,[4] Kyle B. Delwiche,[9] Eoghan P. Reeves,[1] Chelsea N. Sutcliffe,[3] Daniel J. Ritter,[10] Jeffrey S. Seewald,[2] Jennifer C. McIntosh,[10] Harold F. Hemond,[9] Michael D. Kubo,[11] Dawn Cardace,[12] Tori M. Hoehler,[11] Shuhei Ono[1]*

Methane is a key component in the global carbon cycle, with a wide range of anthropogenic and natural sources. Although isotopic compositions of methane have traditionally aided source identification, the abundance of its multiply substituted "clumped" isotopologues (for example, $^{13}CH_3D$) has recently emerged as a proxy for determining methane-formation temperatures. However, the effect of biological processes on methane's clumped isotopologue signature is poorly constrained. We show that methanogenesis proceeding at relatively high rates in cattle, surface environments, and laboratory cultures exerts kinetic control on $^{13}CH_3D$ abundances and results in anomalously elevated formation-temperature estimates. We demonstrate quantitatively that H_2 availability accounts for this effect. Clumped methane thermometry can therefore provide constraints on the generation of methane in diverse settings, including continental serpentinization sites and ancient, deep groundwaters.

Carbon ($^{13}C/^{12}C$) and hydrogen (D/H) isotope ratios of methane are widely applied for distinguishing microbial from thermogenic methane in the environment (*1*–*7*), as well as for apportioning pathways of microbial methane production (*8*–*10*). This bulk isotope approach, however, is largely based on empirical observations, and different origins of methane often yield overlapping characteristic isotope signals (*3*, *7*, *11*–*13*). Beyond conventional bulk isotope ratios, it has become possible to precisely measure the abundance of multiply substituted "clumped" isotopologues (e.g., $^{13}CH_3D$) (*14*, *15*). In particular, the abundance of clumped isotopes makes it possible to obtain information about the temperature at which C–H bonds were formed or last equilibrated (*14*) (fig. S1). Formation temperatures of both thermogenic and microbial methane in natural gas reservoirs can be estimated on the basis of clumped isotopologues (*16*). The mechanisms by which isotopologues attain distributions consistent with thermodynamic equilibrium, however, remain unclear because bulk methane isotopes ($\delta^{13}C$ and δD) often reflect kinetic isotope fractionations (*13*, *17*), and H isotope exchange between methane and water is sluggish (*18*).

To test whether clumped methane thermometry can be widely applied for methane sources beyond natural gas reservoirs, we examined

methane samples from diverse systems, including lakes, wetlands, cow rumen, laboratory cultures of methanogenic microbes, and geological settings that may support abiogenic methane production. We used a recently developed tunable laser spectroscopy technique (*14*, *19*) to measure the relative abundances of four methane isotopologues ($^{12}CH_4$, $^{13}CH_4$, $^{12}CH_3D$, and $^{13}CH_3D$).

Our measurements for dominantly thermogenic gases from the Marcellus and Utica shales (*1*, *20*) yielded $\Delta^{13}CH_3D$-based temperatures of 147^{+25}_{-22}°C and 160^{+29}_{-25}°C, respectively. The clumped isotope temperature for the Marcellus Shale sample is comparable to, although slightly lower than, estimates by Stolper *et al.* (*16*) of 179° to 207°C (Fig. 1). In addition, microbial methane in pore waters and gas hydrates from northern Cascadia margin sediments (*3*) and from wells producing from coal seams in the Powder River Basin (*2*, *21*) yielded $\Delta^{13}CH_3D$ temperatures of 12° to 42°C and 35° to 52°C, respectively. These are consistent with their expected low formation temperatures. Furthermore, thermogenic methane sampled from a hydrothermal vent in the Guaymas Basin, Gulf of California (*6*), yielded a $\Delta^{13}CH_3D$ temperature of 326^{+170}_{-95}°C, within error of the measured vent temperature (299°C) (*22*). Therefore, our data provide independent support of the hypothesis that $^{13}CH_3D$ abundance reflects the temperature at which methane is generated in these sedimentary basins (*16*).

In contrast, we found that methane sampled from lakes, a swamp, and the rumen of a cow carries $^{13}CH_3D$ signals that correspond to anomalously high $\Delta^{13}CH_3D$ temperatures (139° to 775°C) (Fig. 1A) that are well above the environmental temperatures (<40°C). Such signals are clearly not controlled by equilibrium. Notably, a positive correlation between $\Delta^{13}CH_3D$ and the extent of D/H fractionation between methane and environmental water [$\varepsilon_{methane/water}$ (*23*) (Fig. 2)] suggests a strong link between isotopologue (i.e., $^{13}CH_3D$) and isotope (D/H) disequilibria. In contrast, the above-mentioned methane samples from sedimentary basins appear to have attained hydrogen isotope equilibrium with associated waters at or near the temperatures indicated by the $\Delta^{13}CH_3D$ data (Fig. 2).

To confirm these observations from the natural environment, we demonstrated that strong disequilibrium $^{13}CH_3D$ signals are also produced by cultures of methanogenic archaea in the laboratory (Fig. 3). Thermophilic methanogens cultured at 40° to 85°C produced methane with $\Delta^{13}CH_3D$ values from +0.5 to +2.3 per mil (‰) (corresponding to $\Delta^{13}CH_3D$ temperatures of 216° to 620°C), and mesophilic methanogens cultured at ambient temperature produced methane with conspicuously "anticlumped" signatures (i.e., values of $\Delta^{13}CH_3D$ <0‰, for which no apparent temperature can be expressed) as low as –1.3‰ (Fig. 3). Methane from cultures is also characterized by large kinetic D/H fractionation with respect to water (*17*, *24*). Because laboratory cultures are grown under optimal conditions (high H_2 and high CO_2), these anticlumped $\Delta^{13}CH_3D$ and low $\varepsilon_{methane/water}$ values are primarily expressions of kinetic isotope effects. Consequently, the distribution of samples with $\Delta^{13}CH_3D$ and $\varepsilon_{methane/water}$ values in Fig. 2 can be explained by microbial methanogenesis operating on a spectrum between fully kinetic (low $\Delta^{13}CH_3D$ and low $\varepsilon_{methane/water}$) and equilibrium (high $\Delta^{13}CH_3D$ and high $\varepsilon_{methane/water}$) end members.

We constructed a mathematical framework to describe the controls on the correlation of $\Delta^{13}CH_3D$ and $\varepsilon_{methane/water}$ signals from hydrogenotrophic methanogenesis. The model largely follows those developed for microbial sulfate reduction (*25*, *26*) and predicts the isotopologue compositions of product methane as a result of a series of enzymatic reactions (fig. S4) (*19*). Using isotope

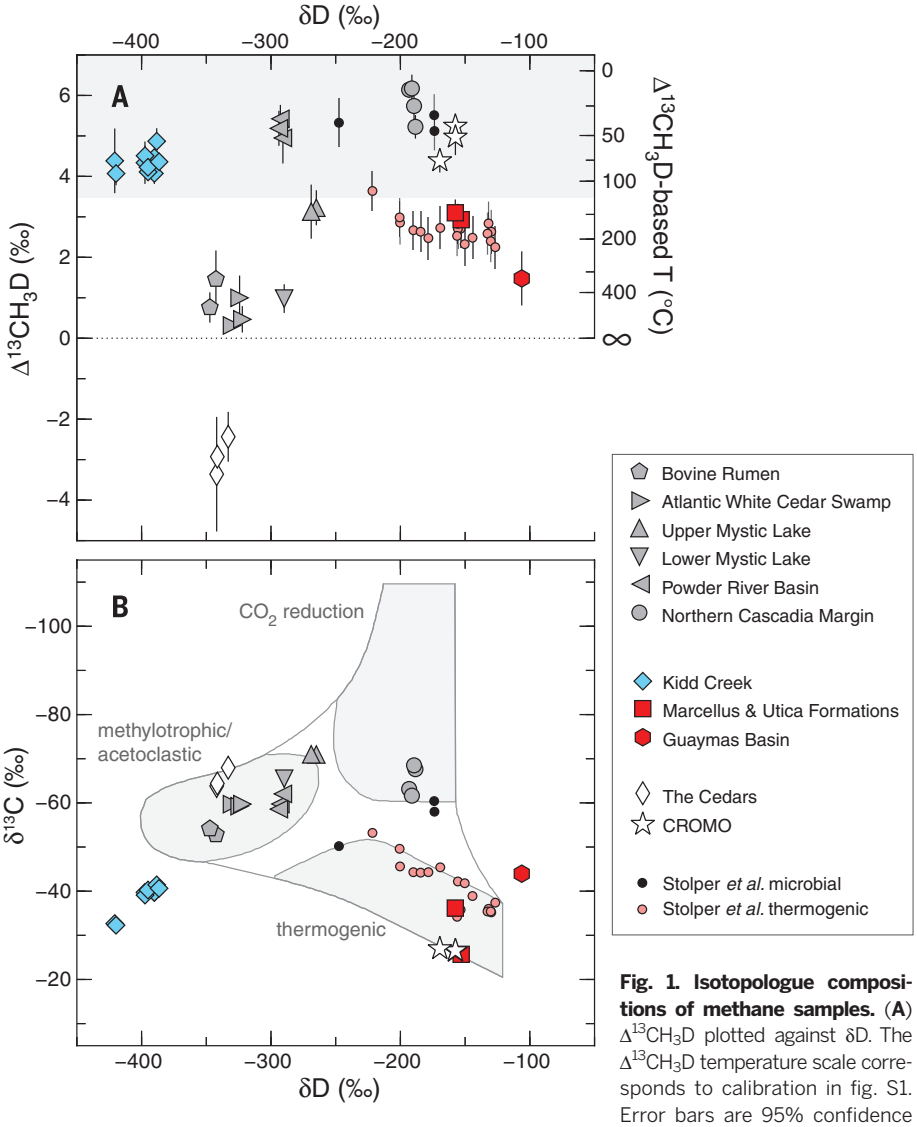

Fig. 1. Isotopologue compositions of methane samples. (**A**) $\Delta^{13}CH_3D$ plotted against δD. The $\Delta^{13}CH_3D$ temperature scale corresponds to calibration in fig. S1. Error bars are 95% confidence intervals (table S1). Data from (*16*) were scaled to their corresponding $\Delta^{13}CH_3D$ values (*15*). The shaded area represents the temperature range within which microbial life has been demonstrated to date (*35*). The dotted line represents $\Delta^{13}CH_3D$ = 0‰ (temperature $T \rightarrow \infty$); data plotting below this line cannot yield corresponding apparent temperatures. (**B**) $\delta^{13}C$ plotted against δD, showing characteristic fields for different methane sources from (*13*).

[1]Department of Earth, Atmospheric and Planetary Sciences, Massachusetts Institute of Technology, Cambridge, MA 02139, USA. [2]Marine Chemistry and Geochemistry Department, Woods Hole Oceanographic Institution, Woods Hole, MA 02543, USA. [3]Department of Earth Sciences, University of Toronto, Toronto, Ontario M5S 3B1, Canada. [4]MARUM Center for Marine Environmental Sciences and Department of Geosciences, University of Bremen, Bremen D-28359, Germany. [5]Department of Microbiology, University of Massachusetts, Amherst, MA 01003, USA. [6]Department of Animal Science, Pennsylvania State University, University Park, PA 16802, USA. [7]U.S. Geological Survey (USGS), Woods Hole Coastal and Marine Science Center, Woods Hole, MA 02543, USA. [8]Department of Earth Sciences, Memorial University of Newfoundland, St John's, Newfoundland and Labrador A1B 3X5, Canada. [9]Department of Civil and Environmental Engineering, Massachusetts Institute of Technology, Cambridge, MA 02139, USA. [10]Department of Hydrology and Water Resources, University of Arizona, Tucson, AZ 85721, USA. [11]NASA Ames Research Center, Moffett Field, CA 94035, USA. [12]Department of Geosciences, University of Rhode Island, Kingston, RI 02881, USA.
***Corresponding author. E-mail: sono@mit.edu**

fractionation factors estimated from theory, experiments, and observations as input parameters (table S3) (*19*), our model reproduces the observed correlation between $\Delta^{13}CH_3D$ and $\varepsilon_{methane/water}$ of natural samples (Fig. 2). The isotopologue compositions of product methane reflect the degree of metabolic reversibility. Fully reversible reactions yield equilibrium end members (*27*), whereas irreversible reactions result in kinetic (disequilibrium) end-member signals. In this model, the reversibility is linked to available free energy (*26*, *27*), in this case expressed as H_2 concentration ($[H_2]$). The model can explain the relationship among $[H_2]$, $\varepsilon_{methane/water}$ (*28*), and $\Delta^{13}CH_3D$ via Michaelis-Menten kinetics and can predict the observed patterns in diverse settings, ranging from marine sediments (low $[H_2]$, high $\Delta^{13}CH_3D$ and $\varepsilon_{methane/water}$) to bovine rumen (high $[H_2]$, low $\Delta^{13}CH_3D$ and $\varepsilon_{methane/water}$) (Fig. 4). We note that mixing of methane sources with different $\delta^{13}C$ and δD values or oxidation of methane could also alter the relationships over the primary signal of microbial methanogenesis (*19*). Likewise, inheritance of clumping signals from precursor organic substrates (e.g., via acetoclastic or methylotrophic methanogenesis) cannot be ruled out entirely and awaits experimental validation.

We showed above that the combination of $\Delta^{13}CH_3D$ and $\varepsilon_{methane/water}$ values provides mechanistic constraints on whether methane was formed under kinetic versus near-equilibrium conditions. Next, we used this framework to place constraints on the origins of methane at two sites of present-day serpentinization in Phanerozoic ophiolites [The Cedars (*29*) and Coast Range Ophiolite Microbial Observatory (CROMO) (*30*)] in northern California, as well as in deep (>2 km below surface) fracture fluids with billion-year residence times in the Kidd Creek mine, Canada (*5*, *31*).

Methane collected from groundwater springs associated with serpentinization at The Cedars yielded anticlumped $\Delta^{13}CH_3D$ signals (–3‰) with low $\varepsilon_{methane/water}$ values (Figs. 1A and 2). The data plot along the microbial (kinetic) trend defined in Fig. 2, supporting a previous hypothesis that methane at The Cedars is being produced by active microbial methanogenesis (*29*). The exceptionally high H_2 concentration (up to 50% by volume in bubbles) at The Cedars indicate the massive excess of electron donors. This, along with severe inorganic carbon limitation [due to high pH (>11) and precipitation of carbonate minerals (*29*)], drives the formation of methane carrying strong kinetic imprints, consistent with the observed anticlumped $\Delta^{13}CH_3D$ signals (Fig. 4).

Despite the similarity in geologic setting, methane associated with serpentinization at CROMO (*30*) revealed very different $\Delta^{13}CH_3D$ values, which correspond to low apparent temperatures (42° to 76°C) and plot close to the equilibrium line (Fig. 2). Although the conventional $\delta^{13}C$ and δD values of methane from CROMO are nearly identical to those of the Utica Shale sample (Fig. 1B), methane at CROMO carries much higher $\Delta^{13}CH_3D$ values (Fig. 1A). The origin of methane at the CROMO site remains unresolved (*30*), but the comparably

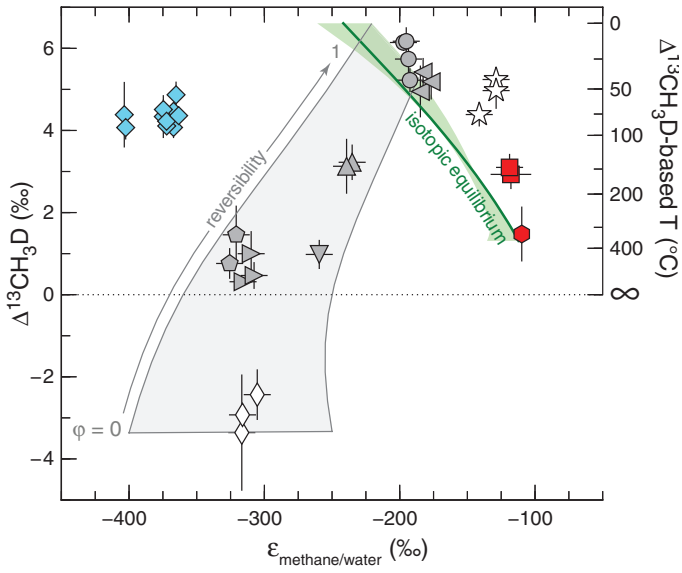

Fig. 2. Extent of clumped and hydrogen isotopic disequilibria in methane. Symbols and vertical error bars are the same as those in Fig. 1. Horizontal error bars represent uncertainties on estimates of $\varepsilon_{methane/water}$ (*23*) (table S4). The solid green curve represents isotopic equilibrium, with the $\varepsilon_{methane/water}$ calibration given by (*36*). Green shading represents ranges of $\varepsilon_{methane/water}$ calibrations from published reports (fig. S3). Gray shading represents model predictions from this study, for microbial methane formed between 0° and 40°C. Metabolic reversibility (φ) increases from bottom (φ = 0, fully kinetic) to top (φ → 1, equilibrium) within this field (*19*).

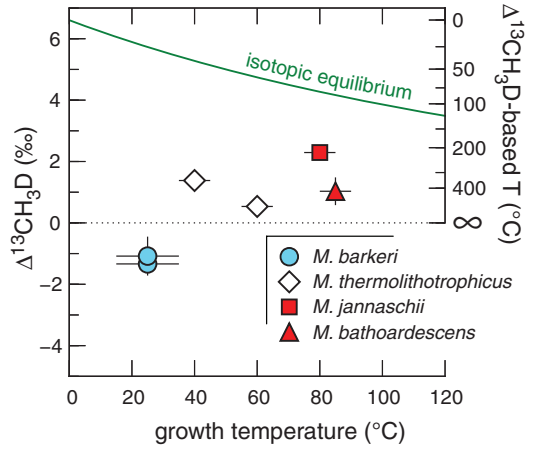

Fig. 3. $\Delta^{13}CH_3D$ values of methane produced by hydrogenotrophic methanogens in batch cultures reflect kinetic effects. Data and error bars are from table S2. The green line represents clumped isotopologue equilibrium (i.e., samples for which $\Delta^{13}CH_3D$ temperature is equal to growth temperature) (fig. S1).

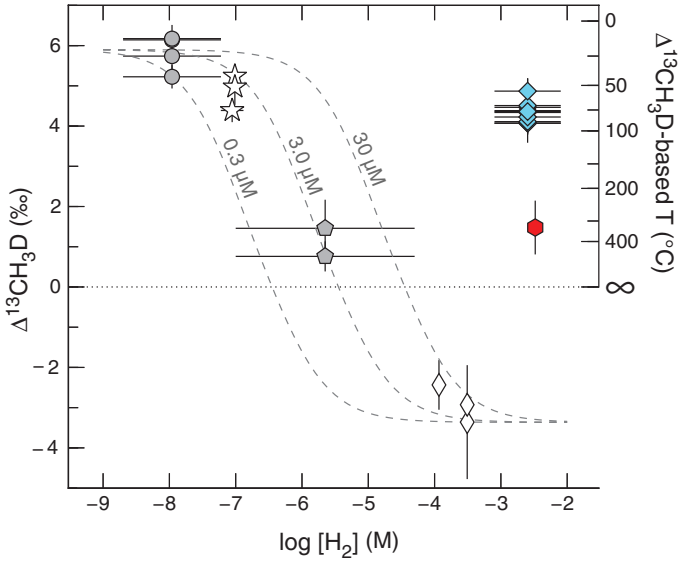

Fig. 4. Relationships between $\Delta^{13}CH_3D$ and H_2 concentration for microbial methane. Symbols and vertical error bars are the same as in Fig. 1. The H_2 data are from table S4; when a range of $[H_2]$ values is given, points are plotted at the geometric mean of the maximum and minimum values. Dashed lines represent model predictions for microbial methane produced at 20°C, calculated using Michaelis-Menten constants (K_M) of 0.3, 3.0, and 30 μM H_2. Data for samples of dominantly nonmicrobial methane from Guaymas Basin and Kidd Creek are plotted for comparison.

high $\Delta^{13}CH_3D$ values at CROMO suggest that methane here could be sourced from a mixture of thermogenic and microbial methane. Alternatively, lower H_2 availability at CROMO, compared with The Cedars (table S4), may support microbial methanogenesis under near-equilibrium conditions (Fig. 4). Regardless, the different isotopologue signatures in methane from CROMO versus The Cedars demonstrate that distinct processes contribute to methane formation in these two serpentinization systems.

Deep, ancient fracture fluids in the Kidd Creek mine in the Canadian Shield (*31*) contain copious quantities of both dissolved methane and hydrogen (*5*). The Kidd Creek methane occupies a distinct region in the diagram of $\Delta^{13}CH_3D$ versus $\varepsilon_{methane/water}$ (Fig. 2), due to strong D/H disequilibria between methane and water (*4*) and low–$\Delta^{13}CH_3D$ temperature signals of 56° to 90°C that are consistent with other temperature estimates for these groundwaters (*4*). Although the specific mechanisms by which the proposed abiotic hydrocarbons at Kidd Creek are generated remain under investigation (*5*, *32*), the distinct isotopologue signals provide further support for the hypothesis that methane here is neither microbial nor thermogenic.

Our results demonstrate that measurements of $^{13}CH_3D$ provide information beyond the simple formation temperature of methane. The combination of methane and water hydrogen-isotope fractionation and $^{13}CH_3D$ abundance enables the differentiation of methane that has been formed at extremely low rates in the subsurface (*3*, *21*, *27*) from methane formed in cattle and surface environments in which methanogenesis proceeds at comparatively high rates (*33*, *34*).

REFERENCES AND NOTES

1. F. J. Baldassare, M. A. McCaffrey, J. A. Harper, *Am. Assoc. Pet. Geol. Bull.* **98**, 341–372 (2014).
2. R. M. Flores, C. A. Rice, G. D. Stricker, A. Warden, M. S. Ellis, *Int. J. Coal Geol.* **76**, 52–75 (2008).
3. J. Pohlman, M. Kaneko, V. Heuer, R. Coffin, M. Whiticar, *Earth Planet. Sci. Lett.* **287**, 504–512 (2009).
4. B. Sherwood Lollar *et al.*, *Geochim. Cosmochim. Acta* **72**, 4778–4795 (2008).
5. B. Sherwood Lollar, T. D. Westgate, J. A. Ward, G. F. Slater, G. Lacrampe-Couloume, *Nature* **416**, 522–524 (2002).
6. J. Welhan, J. Lupton, *Am. Assoc. Pet. Geol. Bull.* **71**, 215–223 (1987).
7. M. J. Whiticar, *Org. Geochem.* **16**, 531–547 (1990).
8. R. A. Burke Jr., C. S. Martens, W. M. Sackett, *Nature* **332**, 829–831 (1988).
9. C. K. McCalley *et al.*, *Nature* **514**, 478–481 (2014).
10. M. J. Whiticar, E. Faber, M. Schoell, *Geochim. Cosmochim. Acta* **50**, 693–709 (1986).
11. G. Etiope, B. Sherwood Lollar, *Rev. Geophys.* **51**, 276–299 (2013).
12. M. Schoell, *Chem. Geol.* **71**, 1–10 (1988).
13. M. J. Whiticar, *Chem. Geol.* **161**, 291–314 (1999).
14. S. Ono *et al.*, *Anal. Chem.* **86**, 6487–6494 (2014).
15. D. A. Stolper *et al.*, *Geochim. Cosmochim. Acta* **126**, 169–191 (2014).
16. D. A. Stolper *et al.*, *Science* **344**, 1500–1503 (2014).
17. D. L. Valentine, A. Chidthaisong, A. Rice, W. S. Reeburgh, S. C. Tyler, *Geochim. Cosmochim. Acta* **68**, 1571–1590 (2004).
18. E. P. Reeves, J. S. Seewald, S. P. Sylva, *Geochim. Cosmochim. Acta* **77**, 582–599 (2012).
19. Materials and methods are available as supplementary materials on *Science* Online.
20. R. Burruss, C. Laughrey, *Org. Geochem.* **41**, 1285–1296 (2010).
21. B. L. Bates, J. C. McIntosh, K. A. Lohse, P. D. Brooks, *Chem. Geol.* **284**, 45–61 (2011).
22. E. P. Reeves, J. M. McDermott, J. S. Seewald, *Proc. Natl. Acad. Sci. U.S.A.* **111**, 5474–5479 (2014).
23. The abundance of $^{13}CH_3D$ is captured by a metric, $\Delta^{13}CH_3D$, that quantifies its deviation from a random distribution of isotopic substitutions among all isotopologues in a sample of methane: $\Delta^{13}CH_3D = \ln Q$, where Q is the reaction quotient of the isotope exchange reaction $^{13}CH_4 + {}^{12}CH_3D \rightleftharpoons {}^{13}CH_3D + {}^{12}CH_4$. The reported δ values are conventional isotopic notation, e.g., $\delta D = (D/H)_{sample}/(D/H)_{reference} - 1$. Mass spectrometric measurements yield Δ_{18}, a parameter that quantifies the combined abundance of $^{13}CH_3D$ and $^{12}CH_2D_2$. For most natural samples of methane, Δ_{18} temperature is expected to be directly relatable to $\Delta^{13}CH_3D$ temperature, as measured by laser spectroscopy. The D/H fractionation between methane and environmental water is defined as $\varepsilon_{methane/water} = (D/H)_{methane}/(D/H)_{water} - 1$.
24. M. Balabane, E. Galimov, M. Hermann, R. Letolle, *Org. Geochem.* **11**, 115–119 (1987).
25. C. Rees, *Geochim. Cosmochim. Acta* **37**, 1141–1162 (1973).
26. B. A. Wing, I. Halevy, *Proc. Natl. Acad. Sci. U.S.A.* **111**, 18116–18125 (2014).
27. T. Holler *et al.*, *Proc. Natl. Acad. Sci. U.S.A.* **108**, E1484–E1490 (2011).
28. R. A. Burke Jr., *Chemosphere* **26**, 55–67 (1993).
29. P. L. Morrill *et al.*, *Geochim. Cosmochim. Acta* **109**, 222–240 (2013).
30. D. Cardace *et al.*, *Sci. Drill.* **16**, 45–55 (2013).
31. G. Holland *et al.*, *Nature* **497**, 357–360 (2013).
32. B. Sherwood Lollar, T. C. Onstott, G. Lacrampe-Couloume, C. J. Ballentine, *Nature* **516**, 379–382 (2014).
33. K. A. Johnson, D. E. Johnson, *J. Anim. Sci.* **73**, 2483–2492 (1995).
34. C. Varadharajan, H. F. Hemond, *J. Geophys. Res.* **117**, G02004 (2012).
35. K. Takai *et al.*, *Proc. Natl. Acad. Sci. U.S.A.* **105**, 10949–10954 (2008).
36. Y. Horibe, H. Craig, *Geochim. Cosmochim. Acta* **59**, 5209–5217 (1995).

ACKNOWLEDGMENTS

We thank J. Hayes, R. Summons, A. Whitehill, S. Zaarur, C. Ruppel, L. T. Bryndzia, N. Blair, D. Vinson, K. Nealson, and M. Schrenk for discussions; W. Olszewski, D. Nelson, G. Lacrampe-Couloume, and B. Topçuoğlu for technical assistance; A. Whitehill, G. Luo, A. Appril, K. Twing, W. Brazelton, A. Wray, J. Oh, A. Rowe, G. Chadwick, and A. Rietze for assistance in the field; R. Michener for the δD_{water} analyses; L. T. Bryndzia (Shell) for providing the shale gas samples; R. Dias (USGS) for sharing the NGS samples; and R. Raiche, D. McCrory, S. Moore (Homestake Mining Co.), the staff of the McLaughlin Natural Reserve, and the well operators for access to samples. Grants from the NSF (EAR-1250394 to S.O. and EAR-1322805 to J.C.M.), N. R. Braunsdorf and D. J. H. Smit of Shell PTI/EG (to S.O.), the Deep Carbon Observatory (to S.O., B.S.L., M.K., and K.-U.H.), the Natural Sciences and Engineering Research Council of Canada (to B.S.L.), and the Gottfried Wilhelm Leibniz Program of the Deutsche Forschungsgemeinschaft (HI 616-14-1 to K.-U.H. and M.K.) supported this study. D.T.W. was supported by a National Defense Science and Engineering Graduate Fellowship. D.S.G. was supported by the Neil a nd Anna Rasmussen Foundation Fund, the Grayce B. Kerr Fellowship, and a Shell-MITEI Graduate Fellowship. Any use of trade, firm, or product names is for descriptive purposes only and does not imply endorsement by the U.S. government. All data used to support the conclusions in this manuscript are provided in the supplementary materials. Author contributions: D.T.W. and S.O. developed the methods, analyzed data, and performed modeling. D.T.W. and D.S.G. performed isotopic analyses. D.S.G., L.C.S., J.F.H., M.K., K.-U.H., and S.O. designed and/or conducted microbiological experiments. D.T.W., D.S.G., B.S.L., P.L.M., K.B.D., A.N.H., C.N.S., M.D.K., D.J.R., J.C.M., D.C., and S.O. designed and/or executed the field-sampling campaigns. D.T.W. and S.O. wrote the manuscript with input from all authors.

SUPPLEMENTARY MATERIALS

www.sciencemag.org/content/348/6233/428/suppl/DC1
Materials and Methods
Supplementary Text
Figs. S1 to S5
Tables S1 to S6
References (*37*–*87*)

5 December 2014; accepted 18 February 2015
Published online 5 March 2015;
10.1126/science.aaa4326

ISOTOPE GEOCHEMISTRY

Biological signatures in clumped isotopes of O_2

Laurence Y. Yeung,[1,2]*† Jeanine L. Ash,[1]*† Edward D. Young[1]

The abundances of molecules containing more than one rare isotope have been applied broadly to determine formation temperatures of natural materials. These applications of "clumped" isotopes rely on the assumption that isotope-exchange equilibrium is reached, or at least approached, during the formation of those materials. In a closed-system terrarium experiment, we demonstrate that biological oxygen (O_2) cycling drives the clumped-isotope composition of O_2 away from isotopic equilibrium. Our model of the system suggests that unique biological signatures are present in clumped isotopes of O_2—and not formation temperatures. Photosynthetic O_2 is depleted in $^{18}O^{18}O$ and $^{17}O^{18}O$ relative to a stochastic distribution of isotopes, unlike at equilibrium, where heavy-isotope pairs are enriched. Similar signatures may be widespread in nature, offering new tracers of biological and geochemical cycling.

Statistical thermodynamics predicts that heavy isotopes will be bound together in a molecule more often than predicted by chance alone, provided the system is at isotopic equilibrium (*1*, *2*). This preference for heavy-isotope pairing and its variation with temperature forms the basis of clumped-isotope thermometry (*3*–*5*), a class of approaches based on precise measurements of molecules containing more than one rare isotope. When isotope-exchange reactions facilitate the equilibration of heavy-isotope pairs, the resulting isotopic distribution

[1]Department of Earth, Planetary, and Space Sciences, University of California, Los Angeles, CA 90095, USA. [2]Department of Earth Science, Rice University, Houston, TX 77005, USA.
*Corresponding author. E-mail: lyeung@rice.edu (L.Y.Y.); jlash@ucla.edu (J.L.A.) †These authors contributed equally to this work.